Article

Improvement of image quality in PET using post-reconstruction hybrid spatial-frequency domain filtering

ARABI, Hossein, ZAIDI, Habib

Abstract

PET images commonly suffer from the high noise level and poor signal-to-noise ratio (SNR), thus adversely impacting lesion detectability and quantitative accuracy. In this work, a novel hybrid dual-domain PET denoising approach is proposed, which combines the advantages of both spatial and transform domain filtering to preserve image textures while minimizing quantification uncertainty. Spatial domain denoising techniques excel at preserving high-contrast patterns compared to transform domain filters, which perform well in recovering low-contrast details normally smoothed out by spatial domain filters. For spatial domain filtering, the non-local mean algorithm was chosen owing to its performance in denoising high-contrast features whereas multi-scale curvelet denoising was exploited for the transform domain owing to its capability to recover small details. The proposed hybrid method was compared to conventional post-reconstruction Gaussian and edge preserving bilateral filters. Computer simulations of a thorax phantom containing three small lesions, experimental measurements using the Jaszczak phantom and clinical [...]

Reference

UNIVERSITÉ
DE GENÈVE

PAPER

Improvement of image quality in PET using post-reconstruction hybrid spatial-frequency domain filtering

View the article online for updates and enhancements.

Physics in Medicine & Biology

Improvement of image quality in PET using post-reconstruction hybrid spatial-frequency domain filtering

Hossein Arabi[1] and Habib Zaidi[1,2,3,4,5]

[1] Division of Nuclear Medicine and Molecular Imaging, Department of Medical Imaging, Geneva University Hospital, CH-1211 Geneva, Switzerland
[2] Geneva University Neurocenter, Geneva University, CH-1205 Geneva, Switzerland
[3] Department of Nuclear Medicine and Molecular Imaging, University of Groningen, University Medical Center Groningen, 9700 RB Groningen, Netherlands
[4] Department of Nuclear Medicine, University of Southern Denmark, DK-500, Odense, Denmark
[5] Author to whom any correspondence should be addressed.

E-mail: habib.zaidi@hcuge.ch

Abstract

PET images commonly suffer from the high noise level and poor signal-to-noise ratio (SNR), thus adversely impacting lesion detectability and quantitative accuracy. In this work, a novel hybrid dual-domain PET denoising approach is proposed, which combines the advantages of both spatial and transform domain filtering to preserve image textures while minimizing quantification uncertainty. Spatial domain denoising techniques excel at preserving high-contrast patterns compared to transform domain filters, which perform well in recovering low-contrast details normally smoothed out by spatial domain filters. For spatial domain filtering, the non-local mean algorithm was chosen owing to its performance in denoising high-contrast features whereas multi-scale curvelet denoising was exploited for the transform domain owing to its capability to recover small details. The proposed hybrid method was compared to conventional post-reconstruction Gaussian and edge preserving bilateral filters. Computer simulations of a thorax phantom containing three small lesions, experimental measurements using the Jaszczak phantom and clinical whole-body PET/CT studies were used to evaluate the performance of the proposed PET denoising technique. The proposed hybrid filter increased the SNR from 8.0 (non-filtered PET image) to 39.3 for small lesions in the computerized thorax phantom, while Gaussian and bilateral filtering led to SNRs of 23.3 and 24.4, respectively. For the experimental Jaszczak phantom, the contrast-to-noise ratio (CNR) improved from 10.84 when using Gaussian smoothing to 14.02 and 19.39 using the bilateral and the proposed hybrid filters, respectively. The clinical studies further demonstrated the superior performance of the hybrid method, yielding a quantification change (the original noisy OSEM image was used as reference in the absence of ground truth) in malignant lesions of −2.4% compared to −11.9% and −6.6% achieved using Gaussian and bilateral filters, respectively. In some cases, the visual difference between the bilateral and hybrid filtered images is not substantial; however the improved CNR score from 11.3 by OSEM to 17.1 and 21.8 by bilateral to the hybrid filtering, respectively, demonstrates the overall gain achieved by the hybrid approach. The proposed hybrid algorithm improved the contrast, SNR and quantitative accuracy compared to Gaussian and bilateral approaches, and can be utilized as an alternative post-reconstruction filter in clinical PET/CT imaging.

1. Introduction

Whole-body PET/CT imaging has become a valuable tool for diagnosis, staging and monitoring response to therapy in clinical oncology. PET commonly suffers from poor spatial resolution and high noise level, which adversely affect lesion detectability and quantitative accuracy. Noise reduction is of paramount importance in protocols with very short acquisition times or low-dosages (e.g. paediatric PET protocols), and dynamic studies with short frames for fast-decaying radiotracers or multiple pass whole-body PET imaging (Karakatsanis *et al* 2016, Yan *et al* 2016, Rahmim *et al* 2018). Statistical reconstruction techniques, such as the maximum likelihood expectation maximization (MLEM) algorithm, are capable of modelling the major physical degrading factors leading to signal loss and noise. However, since image reconstruction is intrinsically ill-posed, these algorithms converge slowly and amplify noise as the iterations proceed (Snyder *et al* 1987). Post-reconstruction filters or statistical reconstruction algorithms with noise modelling are employed to enhance the signal-to-noise-ratio (SNR) in PET images by imposing homogeneity of neighbouring voxels (Nuyts and Fessler 2003, Nuyts *et al* 2005, Qi and Leahy 2006, Reader and Zaidi 2007). However, these methods overlook the fact that tracer uptake can vary abruptly from one voxel to another for prominent signals emanating from malignant lesions or boundaries of organs/tissues. This can lead to smoothing out important signals and meaningful features (Mohammed 2008). In spite of improvement in SNR owing to substantial noise reduction, increased bias in quantification of radiotracer uptake is observed, particularly over sharp edges.

A potential solution to this problem is to use edge-preserving filters in the spatial domain, such as the bilateral (Elad 2002), total variation minimization (Sawatzky *et al* 2008) and anisotropic diffusion filters (Perona and Malik 1990), which are capable of suppressing noise while preserving prominent signals. These approaches rely on the estimation of the prominent boundaries to penalize smoothing factors over the edges. This task can be more effectively achieved by exploiting the complementary information provided by high resolution anatomical images available on multi-modality imaging systems, assuming that the exact boundaries of lesions or organs can be extracted from anatomical images to enhance the performance of edge-preserving filters (Lehovich *et al* 2009, Vunckx *et al* 2012). However, anatomical boundaries do not always coincide with boundaries on emission images and, as such, inaccurate anatomical priors may cause artefacts and quantification bias in corresponding PET images (Vunckx *et al* 2012).

Alternatively, PET denoising techniques based on noise discrimination in the frequency domain through for example wavelet or curvelet transforms have been demonstrated to improve both the quantitative and qualitative aspects of noise filtration (Turkheimer *et al* 2000, Shih *et al* 2005). The curvelet transform (CT) features high sensitivity to anisotropic elements due to superior directional sensitivity over wavelet transform. This feature enables the capture of additional geometrical information, in particular for anisotropic structures, and consequently more accurate image representation (Shan *et al* 2009, Le Pogam *et al* 2013). The curvelet transform provides a sparse representation of structures with the second-order differentiable singularities, where edges are represented with much fewer coefficients in comparison with wavelets for a given accuracy (Shan *et al* 2009).

Overall, the image denoising task can be operated either in the spatial domain using edge preserving methods or in the transform (frequency) domain using curvelet or wavelet shrinkage. Spatial domain methods preserve strong features, such as prominent edges; however they have suboptimal performance to recover low-contrast details (Knaus and Zwicker 2013). Frequency domain techniques, as opposed to spatial domain methods, excel in preserving low-contrast details and textures while suffering from inaccurate edge denoising where some Gibbs ringing artefacts can be observed near strong edges (Le Pogam *et al* 2013, Boashash 2015). The idea here is to take advantage of both spatial and transfer domain filtering to accomplish artefact free denoising while preserving low-contrast features as was explored earlier on natural images (Knaus and Zwicker 2013, 2014, Pierazzo *et al* 2014, Pierazzo and Facciolo 2017). For the spatial domain denoising, we chose non-local mean (NLM) approach, which reduces noise by calculating the weighted average of voxels based on similarities between two patches of voxels. NLM was reported to outperform other edge preserving filters, particularly for white Gaussian noise (Brox *et al* 2008, Chan *et al* 2014). For the frequency domain, we used the curvelet-based coefficients shrinkage, which preserves details well.

The aim of this work is to evaluate a hybrid denoising algorithm that incorporates spatial and frequency domain filtering to enhance the SNR of PET images. The performance of the proposed approach was assessed using simulated, experimental and clinical whole-body PET/CT studies against the conventional Gaussian filter and edge preserving bilateral filter (Hofheinz *et al* 2011).

2. Materials and methods

2.1. Spatial-frequency domain filtering

The objective of hybrid spatial-frequency domain filtering is to restore the noise contaminated PET image f to its original uncorrupted image $\widetilde{Im}$ assuming a noise distribution with a stationary variance. A hybrid method

combining the advantages of both spatial and frequency domains can outperform each of them applied separately. To this end, the image can be filtered separately in two layers, in which the spatial domain layer retrieves the high contrast features whereas the transform domain recovers the low-contrast structures of the image. For the spatial domain denoising, edge preserving methods are highly preferable, and as such, the NLM filter was devised for the high contrast layer. Given the noisy nature of PET images, the prominent edges of the images are first restored in the high contrast layer and then the residual image (defined as the subtraction of spatial domain filtered image from the noisy image as formulated in equation (2)) is passed through the transform domain layer. Since the high contrast features are already denoised, the low-contrast (transform domain) layer is designed to suppress noise on residual images, which predominantly contains medium/low contrast patterns. For the low-contrast layer, a multi-scale decomposition approach based on the curvelet transform was adopted. Image decomposition via the curvelet features high sensitivity to anisotropic elements and directional structures which enable the extraction of additional geometrical information and more accurate image analysis compared to the wavelet transform (Shan *et al* 2009).

The wavelet transform employs basis functions representing both spatial frequency and location. The curvelet transform goes beyond this by utilising basis functions that are also localized in orientation (Starck *et al* 2002). The curvelet transform differs from the wavelet transform in the sense that the degree of the localisation in orientation varies with scales. Wavelets can only capture limited directional information including horizontal, vertical and diagonal features (Shukla and Changlani 2013). These linear directions have limitations and might fail to capture effective directional information in noisy images. However, the curvelet transform captures directional information of an image based on multiple radial directions in the frequency domain. Therefore, the curvelet transform exhibits very high directional sensitivity (anisotropy) as opposed to the wavelet transform with highly isotropic elements (Starck *et al* 2002). The first generation curvelet transform (Starck *et al* 2002) was chosen for frequency domain layer due to its high directional sensitivity and redundancy properties. A number of related publications compared the effectiveness of the wavelet and curvelet transforms to encode the image features in the transform domain and to discriminate genuine signals from noise. They unanimously reported that the wavelet transform is not capable of efficiently representing lines or curvilinear structures, such as edges in the transform domain. Conversely, the ability of the curvelet transform to capture the directionality of image structures (e.g. curves, lines and edges) enables to represent features using fewer coefficients at different scales (Dettori and Semler 2007, Shan *et al* 2009, Shukla and Changlani 2013). This merit of the curvelet transform allows more efficient discrimination between noise and signal due to the redundancy in terms of edges representation in the transform domain. Given the residual image denoised by transfer domain filter, the estimation of the original image can thus be achieved by the sum of the high and low contrast layers outputs. Figure 1 illustrates a block diagram of the hybrid filtering algorithm (figure 1(A)) as well as an anecdotal representation of the filter performance on a 1D signal (figure 1(B)).

2.1.1. Spatial domain filter

The NLM filter was chosen for spatial domain denoising and high contrast feature preservation (Buades *et al* 2005). The NLM (equation (1)) estimates the original/denoised pixel H_i by calculating the average of the entire pixels f_k within a search window (denoted by Ω) weighted by the similarity of surrounding patches of pixels p centred at i and k.

$$H_i = \frac{1}{N_i} \sum_{k \in \Omega_i} f_k w(i,k)$$

$$w(i,k) = \exp\left(-\frac{\|v(p_i) - v(p_k)\|^2}{h^2}\right) v(p_i) = (f_i, \ i \in p_i)$$

$$\|v(p_i) - v(p_k)\|^2 = \sum_{n=1}^{|p|} \left(f_{i(n)} - f_{k(n)}\right)^2$$

$$N_i = \sum_{k \in i} w(i,k) = \sum_{k \in i} \exp\left(-\frac{\|v(p_i) - v(p_k)\|^2}{h^2}\right) \tag{1}$$

$w(i,k)$ represents the weight measuring the similarity between the patches p_i and p_k normalized by N_i (summation of all weighting factors for the target voxel (i) located at the center of searching window (Ω)) to ensure that w ranges from 0 to 1. $|p|$ denotes the patch size for measurement of the similarity with a fixed size of 4×4. The patches of pixels p should be located within the search window (Ω) with a fixed size of 16×16. Typically, the similarity is measured using a decreasing function of the Euclidean distance $\|.\|^2$ between patches of pixels (Buades *et al* 2005). The weighting factors contribute significantly in equation (1) to pixels with similar surrounding pattern to that of the target pixel. The weighting factors can be adjusted by h parameter which determines the decay of the exponential function and normally is set empirically by the user to achieve the desirable degree of smoothness. In case the noise amplitude becomes comparable to the PET signal, the weights corrupted by the noise can adversely affect the smoothing performance of the NLM filter. In this regard, the weighting factors are estimated from a median filtered version of the noisy image to improve the robustness of similarity measurement. The following
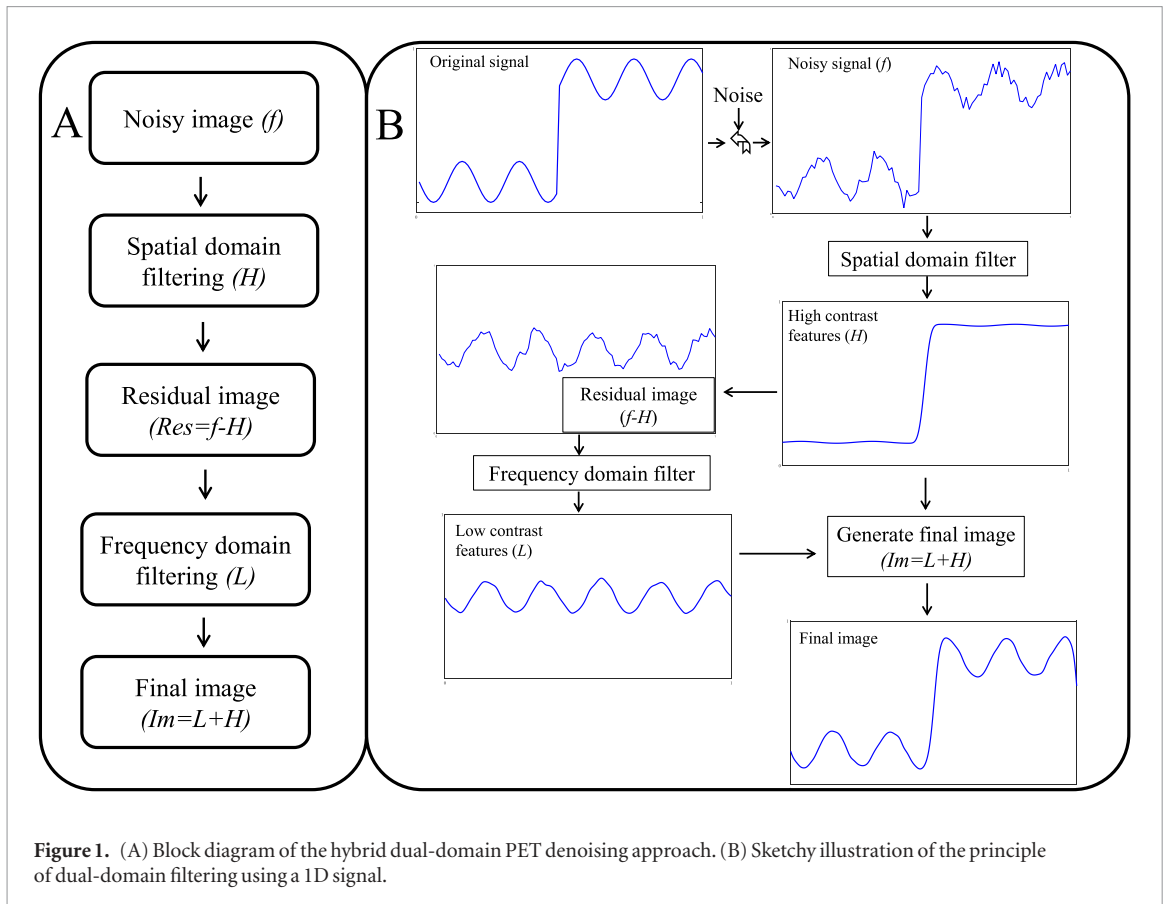
Figure 1. (A) Block diagram of the hybrid dual-domain PET denoising approach. (B) Sketchy illustration of the principle of dual-domain filtering using a 1D signal.

steps were implemented to perform NLM filtering. Initially, given a noisy input PET image, a median filter is applied to generate the median filtered version of the input image. Thereafter, all the weighting factors $w(i, k)$ formulated in equation (1) are calculated on the median filtered version. In the next step, the calculated weighting factors are used to perform the final step of the NLM filtering process on the input noisy image (f_k) to generate the original/denoised pixel H_i. Accordingly, the f_k voxels (first line in equation (1)) are taken from the input noisy image while the weighting factors $w(i, k)$ are calculated on the median filtered version of the image.

2.1.2. Frequency domain filter

The 1D wavelet transform provides excellent sparse representation of the isotropic points (image features with uniformity in all directions) in the spatial domain; however, in higher dimensions (2D or 3D), the wavelet transform results in suboptimal representation of the images with anisotropic contents due to the poor encoding/transformation of the curves, lines and edges where the non-uniform orientation of image features is ignored (Easley *et al* 2008). Recently, the curvelet transform has been employed to address this issue since a more accurate image representation is achievable due to its high directional sensitivity (Hyder and Sukanesh 2011). The curvelet is a multi-scale and multi-directional transform which generates elements indexed by direction, scale and position parameters in the spatial and frequency domains (Starck *et al* 2002). In this study, the first generation curvelet transform was employed, which applies a series of ridgelet analysis and the radon transform. The discrete curvelet utilizes the wavelet transform to decompose the image into a set of wavelet bands to be processed by local ridgelet transform using different block sizes for each scale level (Shan *et al* 2009). Given the image smoothed by a spatial domain filter (H), the residual image to be processed by the curvelet transform is obtained from equation (2):

$$\text{Res} = f - H \tag{2}$$

where f is the initial noisy image. The residual image is then decomposed by the curvelet transform to obtain the curvelet coefficients c_j. Assuming that c_j is the noisy observation of the original image coefficients s_j and the noise samples are denoted by ε_j, we can write:

$$c_j = s_j + \varepsilon_j$$

where $c_j = (c_{1j}, c_{2j})$, $s_j = (s_{1j}, s_{2j})$, $\varepsilon_j = (\varepsilon_{1j}, \varepsilon_{2j})$ and j denotes the number of curvelet coefficients. Here, c_{2j} represents the parent of c_{1j} curvelet coefficient at the same position but at the next coarser scale (supplementary figure 1 (stacks.iop.org/PMB/63/215010/mmedia)). Equation (3) represents the standard MAP estimation of the s considering the corrupted observation c. The index j is dropped to improve readability of the equations.

$$\widehat{s}(c) = \underset{s}{\operatorname{argmax}} \Pr(s|c)$$
$$\widehat{s}(c) = \underset{s}{\operatorname{argmax}} \left[\Pr(c-s) \cdot \Pr(s) \right]. \tag{3}$$

If we assume a non-Gaussian bivariate probability density function (Le Pogam *et al* 2013, Boashash 2015) for the coefficients and their corresponding parents as:

$$\Pr(s) = \frac{3}{2\pi\sigma^2} \exp\left(-\frac{\sqrt{3}}{\sigma} \sqrt{s_1^2 + s_2^2} \right).$$

Then the MAP estimator of the s_1 can be written as Sendur and Selesnick (2002):

$$\widehat{s}_1 = \frac{\left(\sqrt{c_1^2 + c_2^2} - \frac{\sqrt{3}\sigma_n^2}{2\pi\sigma^2} \right)_+}{\sqrt{c_1^2 + c_2^2}} \ c_2. \tag{4}$$

In order to solve equation (4), a prior knowledge of the noise variance σ_n^2 and the marginal variance σ^2 for each curvelet coefficient is needed which can be estimated using surrounding coefficients of the jth coefficient. Let us define $M(j)$ as the entire coefficients neighbouring the jth coefficient as illustrated in supplementary figure 1. The neighbouring window size is a free parameter to be optimized for the peak performance of the curvelet filtering. The noise variance σ_n^2 can be estimated from the finest scale of curvelet coefficients (HH subband) (Donoho and Johnstone 1994) as:

$$\widehat{\sigma}_n^2 = \frac{\operatorname{median}(|c_1|)}{0.6745} \ c_1 \ \in \text{subband HH}. \tag{5}$$

Considering $\sigma_c^2 = \sigma^2 + \sigma_n^2$, the marginal variance of the noisy observations c_1 and c_2 can be empirically calculated using equation (6). It should be noted that the zero mean noise (ε_j) is added to the original image coefficients (s_j) and c_1 and c_2 are modelled as having zero mean due to the bivariate shrinkage function in equation (4).

$$\widehat{\sigma}_c^2 = \frac{1}{|M|} \sum_{c_i \in M} c_i^2. \tag{6}$$

Here $|M|$ denotes the size of the neighborhood $M(j)$, representing a free parameter whose optimal size was estimated using the computer simulations described in section 2.2. Given $\widehat{\sigma}_c^2$, σ can be calculated as Sendur and Selesnick (2002):

$$\widehat{\sigma} = \sqrt{(\widehat{\sigma}_c^2 - \widehat{\sigma}_n^2)_+} \tag{7}$$

After obtaining the denoised curvelet coefficients s_j, the inverse curvelet transform is applied and the final smoothed image (Im) is created by computing the summation of spatial (H) and frequency domain (L) outputs.

$$\text{Im} = L + H$$

The curvelet and NLM filters were implemented in MATLAB environment (2015a MathWorks, Inc., Natick, Massachusetts, United States). Considering a search window size of 16×16 for NLM filtering, the computation time of the proposed hybrid filter did not exceed 15 s (using a double CUP core) for a whole-body PET study, which makes it feasible for clinical practice.

2.2. Simulation, experimental and clinical PET/CT studies

The proposed hybrid method was compared to Gaussian and edge preserving bilateral post-reconstruction filters using computer simulations, experimental phantom measurements and clinical studies.

2.2.1. Computer simulations

The Jaszczak phantom consists of a homogeneous cylinder (100 mm radius and 180 mm length) containing six spheres of different diameters (11, 14, 17, 22, 28 and 33 mm). A 3D digital phantom modelling an ^{18}F-FDG scan of the Jaszczak phantom was developed with matrix size of $256 \times 256 \times 100$ having a voxel size of 2 mm^3 (supplementary figure 2). The spheres were simulated with two levels of contrast, high and medium, corresponding to 8:1 and 5:1, respectively. The homogeneous background was assigned an activity concentration of 2 kBq ml^{-1} whereas the spheres were assigned an activity concentration of 10 and 16 kBq ml^{-1} to mimic medium and high contrast situations, respectively. Only photon attenuation was considered in the simulation with image reconstruction performed in 2D mode. In this work, the finite resolution of the PET scanner was accounted for by blurring the projections using a Gaussian filter with full-width at half-maximum (FWHM) of 6 mm. As mentioned in *frequency domain filter* section, curvelet filtering contains a neighbouring window $M(j)$

parameter to be optimized to reach its peak performance. To this end, different window sizes were compared using the simulated Jaszczak phantom for 12 setups (two contrast levels and six noise realizations). The generated noise realizations produced a noise variance ranging from 0.001 to 0.10 in the background when the image is normalized in the range 0–1. Supplementary figure 3 depicts the application of solely curvelet filtering on the computer phantom while the neighbouring window varies from 3 to 13 with a step of 2. A window size of 7 was chosen for the rest of the study since this led to the highest SNR and minimum bias.

In addition to the Jaszczak phantom, a digital thorax phantom bearing three small lesions of size $10 \times 10 \times 10$ mm was simulated using the same simulation setup with a matrix size of $256 \times 256 \times 100$ and a voxel size of 2 mm^3. The body content (soft tissue) and lung region of the phantom had attenuation coefficients of 0.1 cm^{-1} and 0.03 cm^{-1}, respectively. The lesions were placed in the lung and soft-tissue regions with three levels of tumour to background ratios: 4:1 for L1, 2:1 for L2 and 3:1 for L3 (Supplementary figure 2). Eleven noise realizations were simulated with added Poisson noise to the projection data by varying the total number of counts. The total number of counts in the sinogram was around 1 M per slice generating a noise variance in the lung region ranging from 0.001 to 0.1. Image reconstruction was performed using OSEM algorithm with four iterations and eight subsets using the Michigan image reconstruction toolbox (MIRT) implemented in Mathwork's Matlab language[6]. It should be noted that similar results were obtained for computer simulations performed with a reconstruction resolution of $4 \times 4 \times 2.5$ mm.

2.2.2. Experimental phantom studies
The physical Jaszczak phantom containing six hot spheres, having diameters of 11.89, 14.43, 17.69, 21.79, 26.82 and 33.27 mm were filled with an activity concentration of 18.4 kBq ml^{-1} while the cylinder (background) was filled with 3.6 kBq ml^{-1} to create a contrast of 5:1. The total injected activity was 22 MBq. The Jaszczak phantom was then scanned on a Biograph mCT PET/CT (Siemens Medical Solutions USA, Knoxville, TN, USA) in list-mode format with a total acquisition time of 30 min. The data were then reconstructed for different time frames corresponding to 10 s, 30 s, 1 min, 3 min, 10 min and 30 min to realize different noise levels. Image reconstruction was performed using OSEM algorithm with four iterations and eight subsets including CT-based attenuation and scatter correction using the e7 tool (Siemens Healthcare, Knoxville, TN) and the embedded single scatter simulation (SSS) algorithm with tail fitting scaling. The reconstructed image matrix consisted of $400 \times 400 \times 45$ voxels with size of $2 \times 2 \times 5$ mm.

2.2.3. Clinical studies
Twelve clinical ^{18}F-FDG PET/CT studies (mean age $\pm$ SD $= 61 \pm 7$ y)were performed on a Biograph 64 True Point scanner (Siemens Healthcare, Erlangen, Germany) for staging of head and neck malignancies following administration of ^{18}F-FDG (371 ± 23 MBq). PET data acquisition was carried out for five to six total bed positions (3 min per bed) resulting in a total acquisition time of 15–18 min. The patient weights ranged from 50 to 91 kg (mean = 65.75 kg). CT-based attenuation correction was performed followed by image reconstruction using the e7 tool (Siemens Healthcare, Knoxville, TN) using ordinary Poisson ordered subset-expectation maximization (OP-OSEM) iterative algorithm and the default parameters used in the clinic (four iterations and eight subsets). The default post-processing Gaussian filtering was deactivated to obtain unfiltered PET images with a matrix of $168 \times 168 \times 205$ voxels having a dimension of $4 \times 4 \times 2.5$ mm^3. Overall, 35 VOIs were defined on malignant lesions where the number of lesions varied only slightly between the patients (mean = 3, range: 2–4). The lesions were located in the liver, lung, and head and neck. The background VOIs were defined in the same regions with the same size (ranging from 0.4 to 18 ml).

2.3. Evaluation strategy
The evaluation of the proposed approach was carried out through comparison with Gaussian and bilateral post-reconstruction filters. 3D Gaussian filter was applied to all studies with a range of kernels from 2 mm to 10 mm FWHM for computer simulations, experimental phantoms and clinical studies. 2D bilateral filtering was performed on a slice by slice basis. The bilateral filter consists of a product of two spatial and intensity domain kernels having Gaussian shapes (Paris *et al* 2009). The spatial and intensity kernels are controlled by two Gaussian standard deviations, σ_{Sp} and σ_{In}, respectively. The standard deviation of the spatial kernel was fixed at 3.8 mm as suggested in Hofheinz *et al* (2011), whereas the intensity standard deviation (σ_{In}) was chosen in such a way that bilateral filtering resulted in comparable standard deviation in soft-tissue region as Gaussian filtering. σ_{In} was set to a range of 0.1–0.5 considering the images normalized to the intensity range of 0–1.

For the Jaszczak (computer and physical) and thorax phantoms, the performance of the different approaches was quantitatively evaluated using the contrast-to-noise ratio (CNR) (Kim *et al* 2015) for various regions of interest (ROIs):

---

[6] http://web.eecs.umich.edu/~fessler/code/index.html.

$$\text{CNR} = \frac{\left| \mu_{\text{signal}} - \mu_{\text{background}} \right|}{\sqrt{\frac{\left| \sigma^2_{\text{signal}} + \sigma^2_{\text{background}} \right|}{2}}}. \tag{8}$$

Here, μ_{signal} and $\mu_{\text{background}}$ denote the mean values of the target and background ROIs in filtered images, respectively, while σ^2_{signal} and $\sigma^2_{\text{background}}$ are the corresponding standard deviations. The same ROIs on target and background regions were defined to have the same number of voxels (supplementary figure 2). Moreover, normalized bias and SNR, as formulated in equations (9) and (10), respectively, were used to assess the performance of the different algorithms.

$$\text{Bias}(\%) = \frac{100}{\text{Lr}} \sum_{i=1}^{\text{Lr}} \frac{\left| (\mu_{\text{signal}_i} - \text{Tl}) \right|}{\text{Tl}} \tag{9}$$

$$\text{SNR} = \frac{\frac{1}{\text{Lr}} \sum_{i=1}^{\text{Lr}} \left(\mu_{(\text{signal})i} - \mu_{(\text{background})i} \right)}{\frac{1}{\text{Bg}} \sum_{j=1}^{\text{Bg}} \sigma_j}. \tag{10}$$

Here Tl is the true intensity value within the ROI and Lr the number of different noise realizations. σ_j denotes the ensemble standard deviation of each voxel j across the noise realizations and Bg is the total number of voxels within the background ROI. For the simulated and experimental studies, the true values of the signals are known and, as such, equation (9) can be used to estimate the bias. For the clinical studies, the mean tracer uptake and standard deviation in the lesion ROIs were computed before and after post-reconstruction filtering. Similarly, the SNR and CNR were calculated for the lesion ROIs using the aforementioned equations. However, the changes after applying the different denoising algorithms were computed using equation (11) considering the unfiltered OSEM image as baseline (Guo *et al* 2003).

$$\text{Change}\,(\%) = \frac{\mu\text{ROI}_{\text{filtered}} - \mu\text{ROI}_{\text{noisy}}}{\mu\text{ROI}_{\text{noisy}}} \times 100\%. \tag{11}$$

Contrast recovery coefficients (RCs) were calculated in the experimental phantom study using equation (12), where μ_{signal} and $\mu_{\text{background}}$ denote measured activity concentrations and Tl and Tb denote actual activity concentrations in the spheres and background, respectively.

$$\text{RC}\,(\%) = \frac{\mu_{\text{signal}} - \mu_{\text{background}}}{\text{Tl} - \text{Tb}} \times 100. \tag{12}$$

To demonstrate the added benefits of combining the spatial and transfer domain, the hybrid filter was compared to each of NLM and curvelet filters separately using the experimental phantom study using SNR, CNR and bias metrics. For all datasets, manually drawn ROIs were placed on unfiltered OSEM images over identified structures such as spheres or lesions and over large homogeneous regions (to estimate the background activity or noise standard deviation), such as the lungs or liver for clinical studies. The same ROIs (shape and size) were placed over each pair of target and background regions. The post-filtering parameters for the different approaches were set to achieve the highest SNR and CNR according to computer simulations and experimental phantom studies. The free parameters were optimized in a general manner (not for a specific count statistics) and the same parameters were adopted for the clinical studies. Different patch sizes and search windows were examined to achieve reasonable compromise between smoothing quality and processing time (in particular for the search window). The sizes of the search window and voxel patch were set to 16×16 and 4×4, respectively. A Gaussian kernel with a FWHM = 8 mm, $\sigma_{\text{Sp}} = 3.8$ mm and $\sigma_{\text{In}} = 0.3$ for the bilateral filter led to peak performance and resulted in similar noise variance in soft-tissues or background for phantom studies.

The evaluation of the clinical studies was performed on PET images reconstructed using the default parameters used in the clinic (four iterations and eight subsets) which involve preset convergence level. To evaluate the performance of the different approaches at varying convergence or contrast levels, the evaluation of the clinical studies was repeated for different iteration numbers ranging from 1 to 8 with a preset number of eight subsets. The CNR values before (unfiltered OSEM) and after post-reconstruction filtering were recalculated for the lesion ROIs at the different iteration numbers.

3. Results

3.1. Computer simulations

The results for the simulated Jaszczak phantom are illustrated in figure 2 for the noise realization leading to a variance of ~1.1. The hybrid approach led to minimum signal and resolution loss contrary to Gaussian and bilateral filters as demonstrated in the residual images (*noisy image—filtered image*). This is also highlighted in the
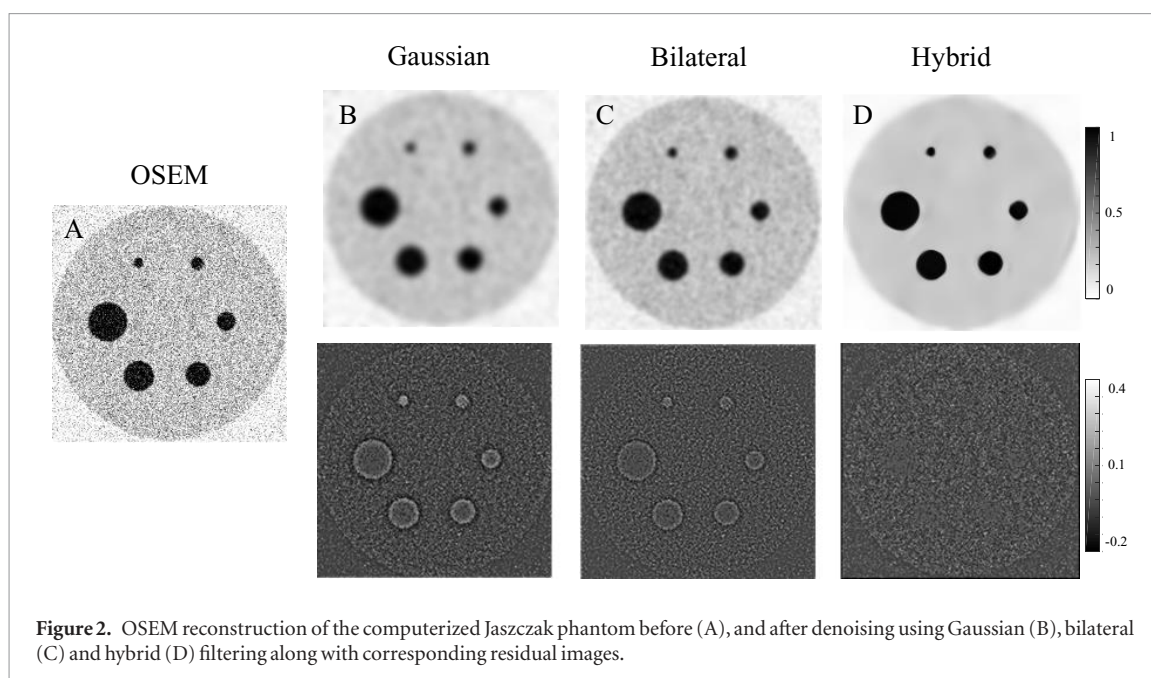
Figure 2. OSEM reconstruction of the computerized Jaszczak phantom before (A), and after denoising using Gaussian (B), bilateral (C) and hybrid (D) filtering along with corresponding residual images.

profiles plotted over the six spheres depicted in figure 3. Gaussian filtering led to significant signal and contrast loss for all spheres, in particular the smaller ones. Bilateral filtering yielded moderate blurring of contours especially for the smallest sphere. Finally, the hybrid approach yielded minimum loss of contrast and blurring compared to the OSEM image. In case of high noise levels, the bilateral and hybrid filters led to higher signal fluctuation (as indicated in figure 3 for 28 and 17 mm spheres); however the hybrid approach was less sensitive. The profiles in figure 3 are plotted for a signal to background ratio of 5:1. The CNR for the simulated Jaszczak phantom with medium (5:1) and high (8:1) contrast is reported in table 1 for the different denoising algorithms. The proposed approach generally provides better CNR values compared to the other denoising algorithms regardless of the noise level and contrast (figure 3). The Gaussian and bilateral filtering failed to improve the CNR for the smallest sphere (ROI 1) particularly for high contrast images. The Gaussian, bilateral and hybrid filtering resulted in a CNR of 7.76, 8.89 and 17.89, respectively; compared to OSEM images (CNR of 14.46).

The results of the thorax phantom containing three small lesions are illustrated in figure 4. Similar to the smallest sphere in the simulated Jaszczak phantom, signal loss and blurring of structures are observed when applying Gaussian filtering which led to a significant loss of resolution compared to the two other approaches, as demonstrated by the profiles illustrated in figure 5. The profiles depict different levels of intensity and contrast loss when applying all three denoising approaches. However, the hybrid approach led to significantly lower resolution loss. The qualitative evaluation was confirmed by the measurement of bias, SNR and CNR of the ROIs drawn on the lesions (supplementary figure 2) reported in table 2. Gaussian filtering yielded significantly increased bias with a maximum value of 36%, while bilateral filtering exhibited better performance and resulted in maximum bias (27%) compared to the one observed on the OSEM image (23%). All filtering approaches led to increased bias compared to noisy images; however, this trend was less severe when using the hybrid approach (maximum bias of 24%).

3.2. Experimental phantom studies

The results for the experimental Jaszczak phantom filtered by the different approaches are illustrated in figure 6. The list-mode PET data obtained from 30 min scan were reconstructed corresponding to different acquisition times to realize different noise levels. Considerable resolution and signal recovery can be observed in images filtered by the hybrid approach (figure 7). The Gaussian filter led to important loss of contrast and signal particularly for the smallest sphere (10 mm), while bilateral and hybrid filtering exhibited superior performance for images with low SNR. According to table 3, the hybrid approach led to lower bias and improved CNR across the spheres with a maximum bias of 31% compared to 36% and 33% for Gaussian and bilateral filtering, respectively. In terms of CNR, all the approaches increased the CNR in proportion to the size of the spheres. However, maximum CNR (24.01) was obtained using the hybrid approach for the largest sphere whereas Gaussian filtering yielded minimum CNR (6.02) for the smallest sphere.

Moreover, table 4 reports the CNR, SNR and bias for the Jaszczak phantom study processed by the proposed hybrid filter and each of the spatial (NLM) and transform (curvelet) domains separately. Representative slices of the Jaszczak phantom acquired with different acquisition times before and after applying the curvelet, NLM and hybrid post-reconstruction filtering are presented in supplementary figure 5.
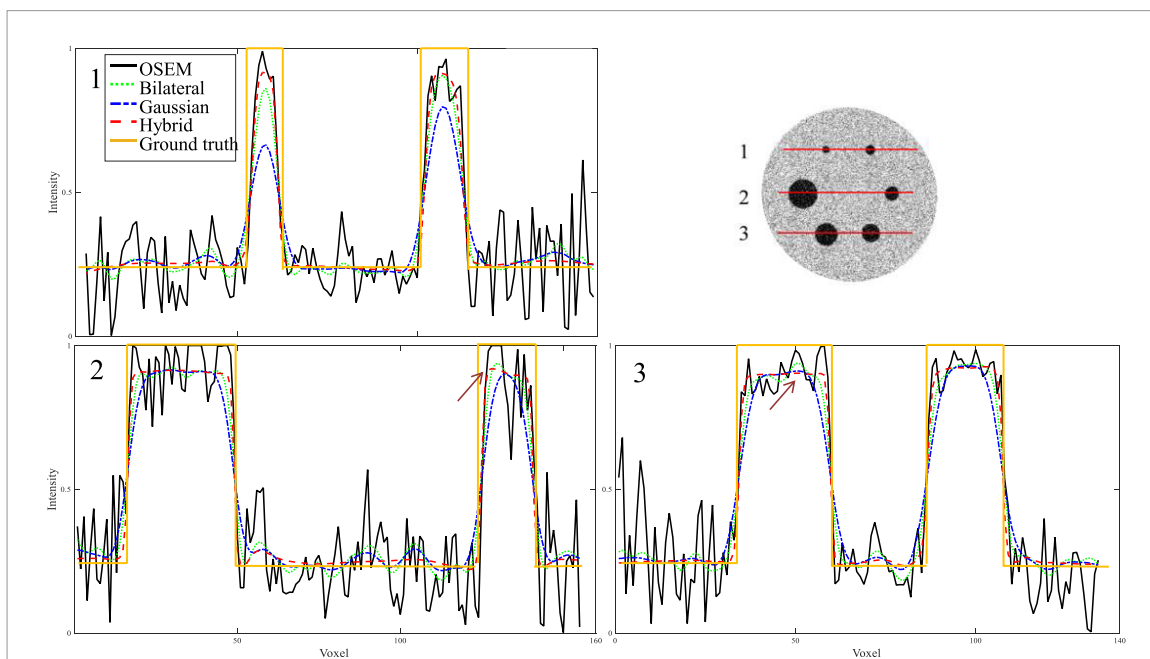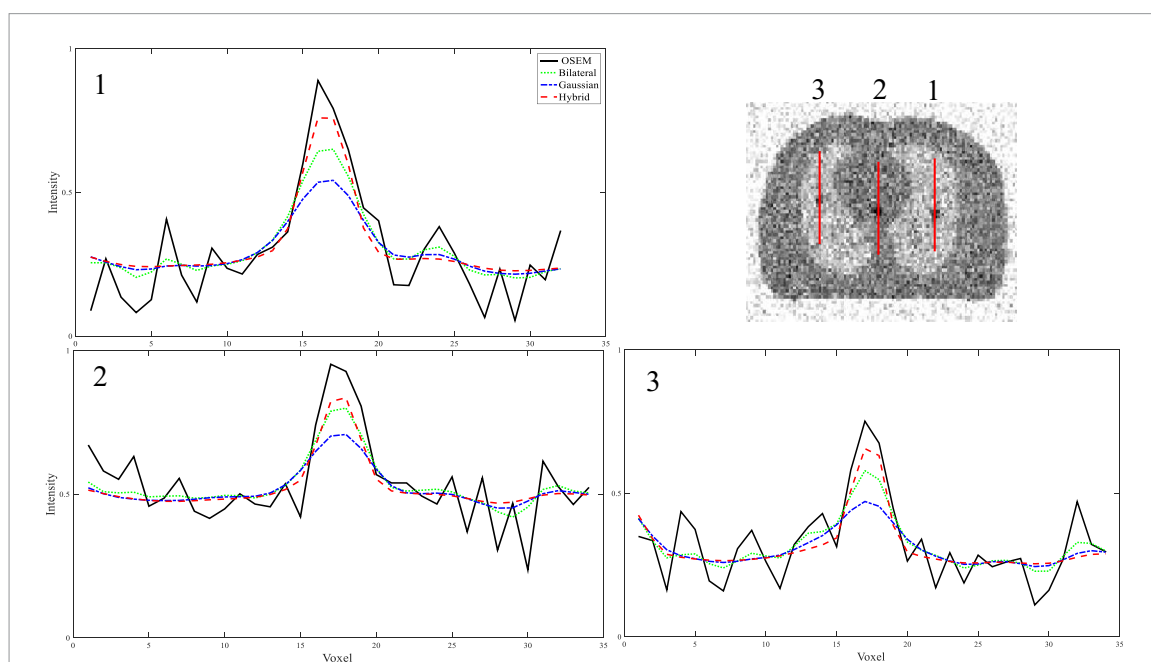
Figure 3. Comparison of horizontal profiles drawn on the six spheres of the computerized Jaszczak phantom with high noise level before and after applying Gaussian, bilateral and hybrid post-reconstruction filtering.

Table 1. Contrast-to-noise ratio (CNR) measured in the different spheres of the simulated Jaszczak phantom at medium (1:5) and high (1:8) signal-to-background ratios. The ROIs are displayed in supplementary figure 2(A).

ROI	Contrast	OSEM	Gaussian	Bilateral	Hybrid
1	Medium	6.34	5.97	6.98	13.65
	High	14.46	7.76	8.89	17.89
2	Medium	4.52	8.56	10.02	15.53
	High	10.70	10.89	12.64	19.01
3	Medium	5.23	11.56	15.03	22.41
	High	11.93	12.11	17.36	25.03
4	Medium	8.50	13.43	16.94	23.11
	High	15.33	13.56	18.63	25.89
5	Medium	7.05	12.40	17.76	23.91
	High	14.19	13.60	18.93	26.19
6	Medium	9.02	13.0	18.00	24.45
	High	15.65	13.87	19.61	27.45
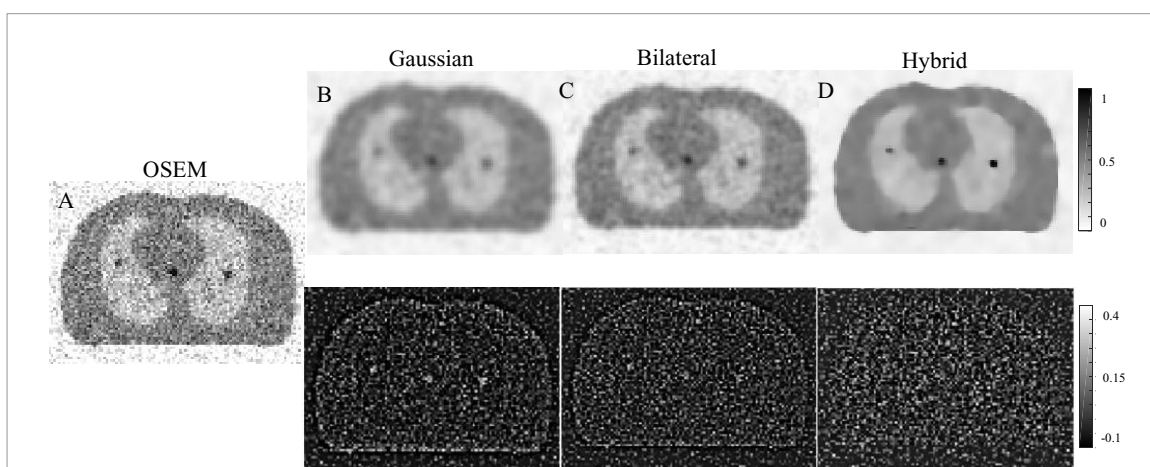
Figure 4. OSEM reconstruction of the computerized thorax before (A), and after denoising using Gaussian (B), bilateral (C) and hybrid (D) post-reconstruction filtering along with corresponding residual images.
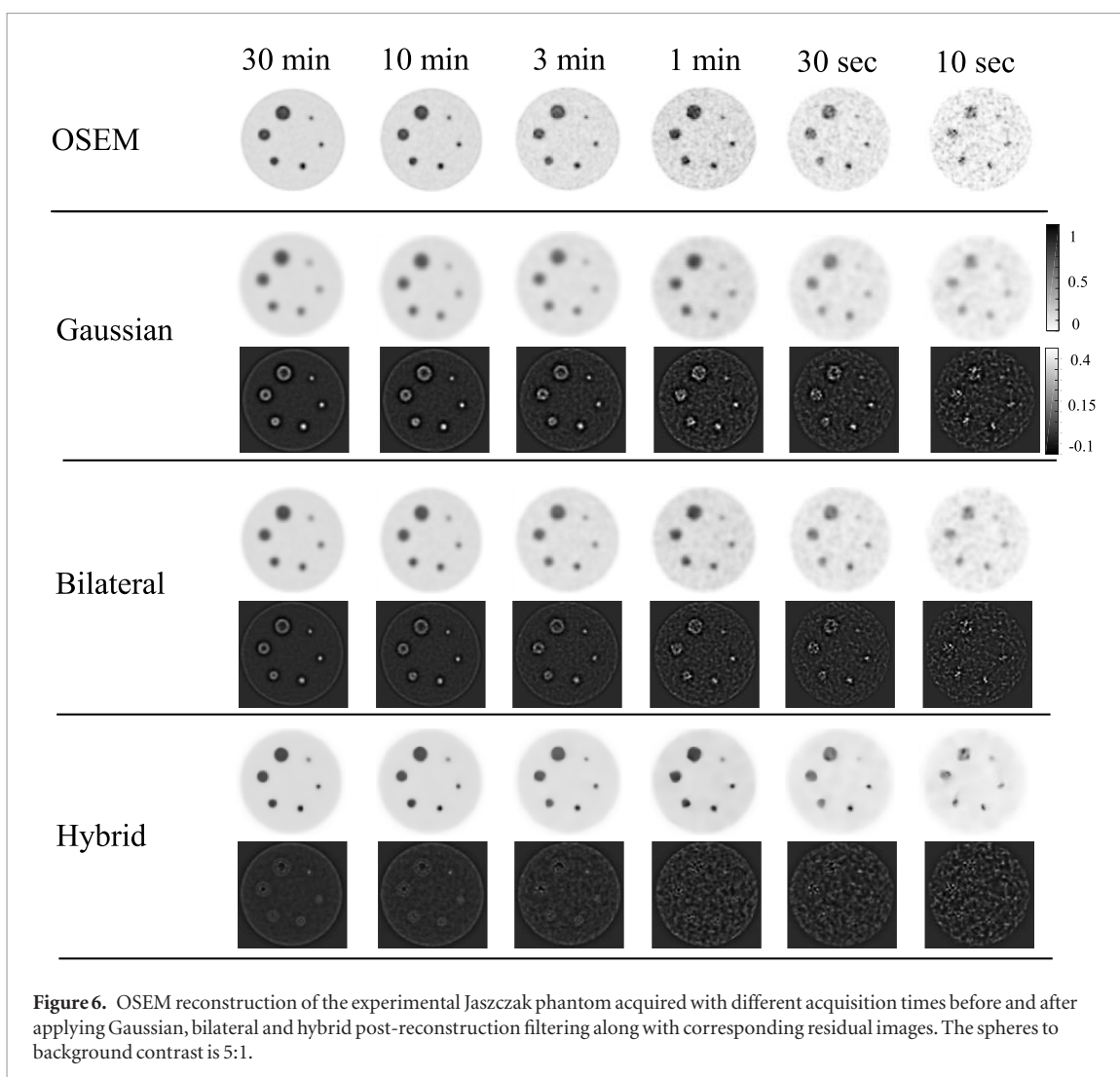
Figure 5. Comparison of vertical profiles drawn on the three lesions of the computerized thorax phantom before and after applying Gaussian, bilateral and hybrid post-reconstruction filtering.

Table 2. Contrast-to-noise ratio (CNR), signal-to-noise ratio (SNR) and quantification bias measured on the three lesions of the computerized thorax phantom. The ROIs are displayed in supplementary figure 2(B).

Lesion		OSEM	Gaussian	Bilateral	Hybrid
L1	Bias (%)	23	36	27	24
	SNR	13	39	41	63
	CNR	5.69	5.08	7.42	13.04
L2	Bias (%)	18	29	25	20
	SNR	4	15	13	26
	CNR	4.95	7.87	9.69	14.77
L3	Bias (%)	14	24	22	17
	SNR	7	16	19	29
	CNR	6.07	12.35	15.98	23.19

3.3. Clinical studies

Qualitatively, the clinical images were efficiently denoised whatever the method used as highlighted in the representative non-small lung cancer clinical study shown in figure 8. Judging based on the residual images; hybrid filtering effectively suppressed the noise with relatively minimal signal loss. The profile plotted on the lung lesion demonstrates that Gaussian filtering led to higher loss of signal and contrast compared to bilateral and hybrid filtering. Similar results are presented in supplementary figure 4 illustrating a patient with a small lesion located in soft-tissue region with lower contrast with respect to the background. The residual images and the plotted profile on the lesion demonstrate the superior performance of the hybrid approach. This is further confirmed by the average change (%) for lesions achieved by the different approaches (table 5). In the absence of ground truth for the clinical studies, the changes (%) were measured against the unfiltered OSEM images. The noise variance in the 35 background VOIs (defined for measurement of CNR and SNR using equations (8) and (10)) ranged from 0.002 to 0.09. In addition to previously calculating CNR at a fixed convergence level in clinical studies, figure 9 illustrates the trend of CNR changes with the number of iterations before (unfiltered OSEM) and after application of post-reconstruction filtering. Representative coronal views of a clinical study reconstructed at different iteration numbers along with vertical profiles through the lesion are presented in supplementary figure 6. The highest lesion to background ratio and CNR occurred at iteration number 4 (eight subsets). As the number of iterations proceeds, the CNR drops drastically primarily owing to the steep increase of noise levels at higher number of iterations. The hybrid approach exhibited superior performance both at low lesion to background ratio (early iterations) and high noise levels (late iterations).

Figure 6. OSEM reconstruction of the experimental Jaszczak phantom acquired with different acquisition times before and after applying Gaussian, bilateral and hybrid post-reconstruction filtering along with corresponding residual images. The spheres to background contrast is 5:1.
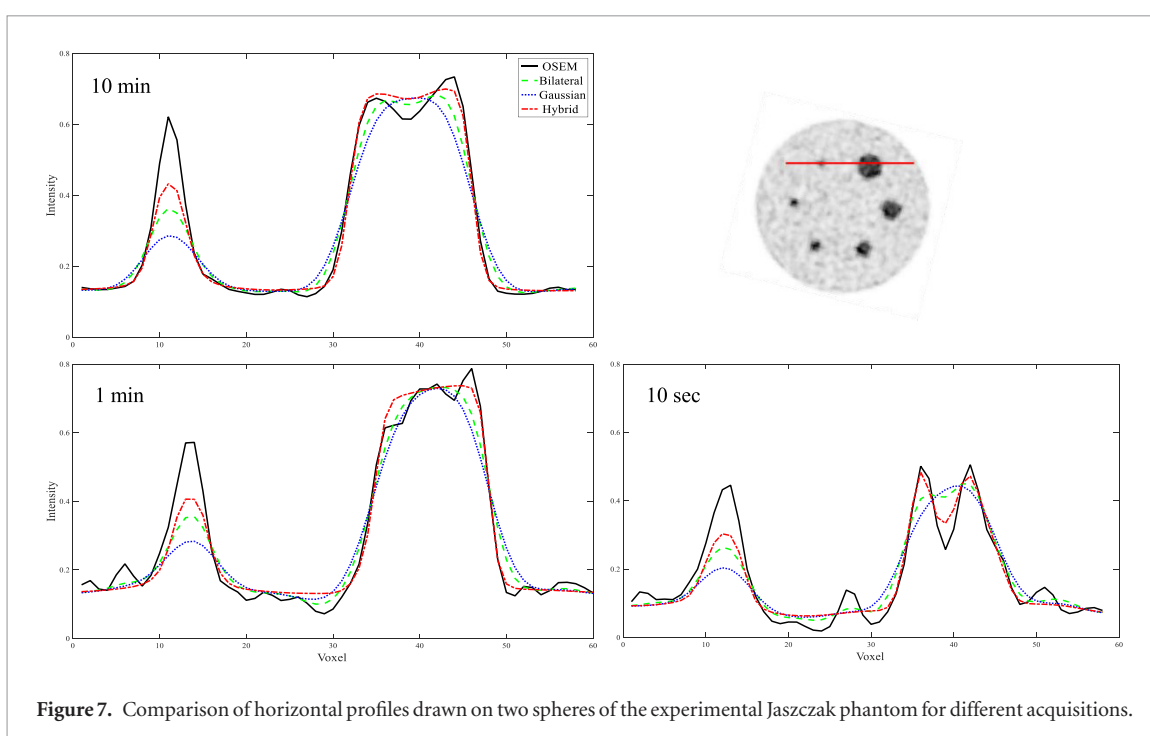
Figure 7. Comparison of horizontal profiles drawn on two spheres of the experimental Jaszczak phantom for different acquisitions.

Table 3. Contrast-to-noise ratio (CNR), signal-to-noise ratio (SNR), contrast recovery coefficient (RC) and quantification bias measured in the different spheres of the experimental Jaszczak phantom (the spheres to background contrast is 5:1) before and after post-reconstruction filtering.

ROI		OSEM	Gaussian	Bilateral	Hybrid
1	Bias (%)	29	36	33	31
	SNR	8	16	19	24
	CNR	5.91	6.02	8.70	13.82
	RC(%)	45	38	41	43
	Bias (%)	27	33	31	30
2	SNR	7	16	18	27
	CNR	6.23	8.12	9.98	12.93
	RC(%)	55	49	51	52
	Bias (%)	25	31	29	28
3	SNR	10	20	23	29
	CNR	8.17	11.15	14.68	20.01
	RC(%)	62	56	59	60
	Bias (%)	25	29	28	27
4	SNR	12	23	28	33
	CNR	9.05	13.90	17.04	22.09
	RC(%)	74	69	71	72
	Bias (%)	24	27	26	25
5	SNR	13	24	28	35
	CNR	8.14	13.11	16.94	23.45
	RC(%)	82	78	79	80
	Bias (%)	22	25	24	24
6	SNR	12	25	30	38
	CNR	9.12	12.73	17.89	24.01
	RC(%)	84	79	81	82

Table 4. Contrast-to-noise ratio (CNR), signal-to-noise ratio (SNR) and quantification bias measured in the different spheres of the experimental Jaszczak phantom (the spheres to background contrast is 5:1) before (unfiltered OSEM) and after post-reconstruction filtering using the hybrid and each of the hybrid filter components (NLM and curvelet) separately.

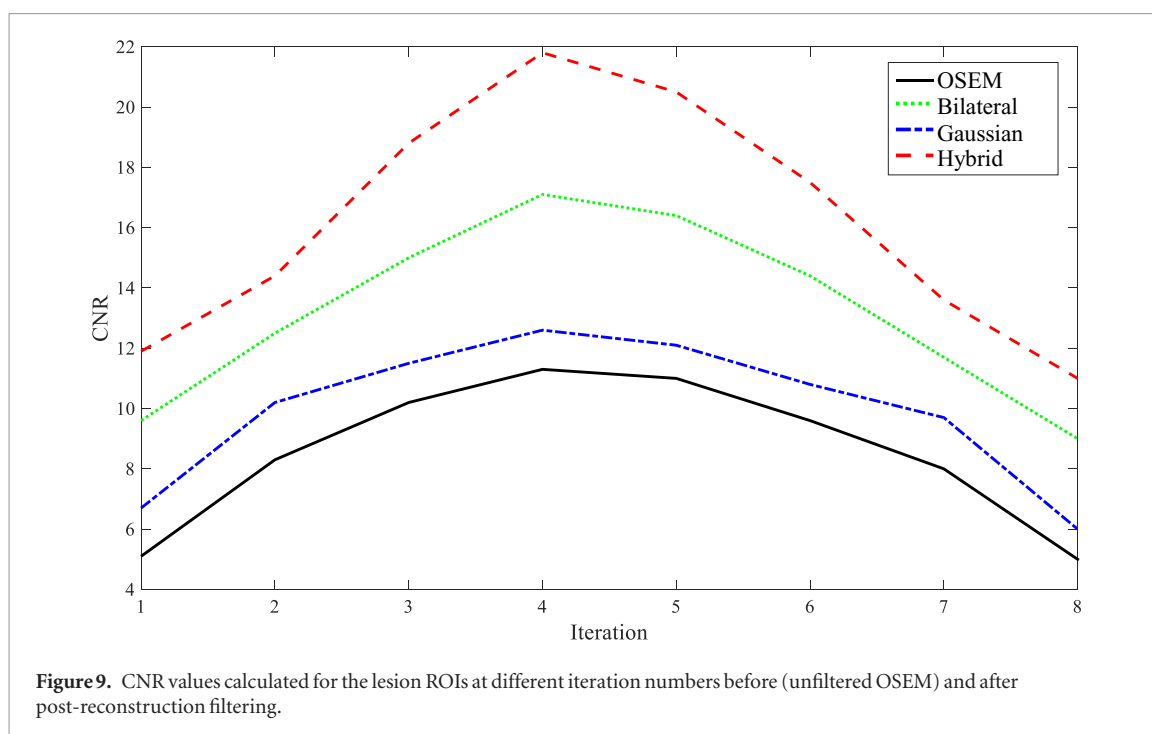| ROI		OSEM	Curvelet	NLM	Hybrid
1	Bias(%)	29.0	31.5	32.0	31.0
	SNR	8	24.8	27.9	28
	CNR	5.91	8.9	12.9	13.82
2	Bias(%)	27	30.7	31.4	30
	SNR	7	24.9	25.7	27
	CNR	6.23	9.8	12.1	12.93
3	Bias(%)	25	28.0	28.9	28.0
	SNR	10	25.6	28.1	29
	CNR	8.17	15.2	17.8	20.01
4	Bias(%)	25	27.1	28.2	27
	SNR	12	26.3	31.3	33
	CNR	9.05	17.3	21.6	23.09
5	Bias(%)	24	25.4	26.9	25
	SNR	13	27.1	31.4	35
	CNR	8.14	18.3	21.1	23.45
6	Bias(%)	22	23.8	25.1	24
	SNR	12	27.3	31.5	38
	CNR	9.12	18.1	22.1	24.01
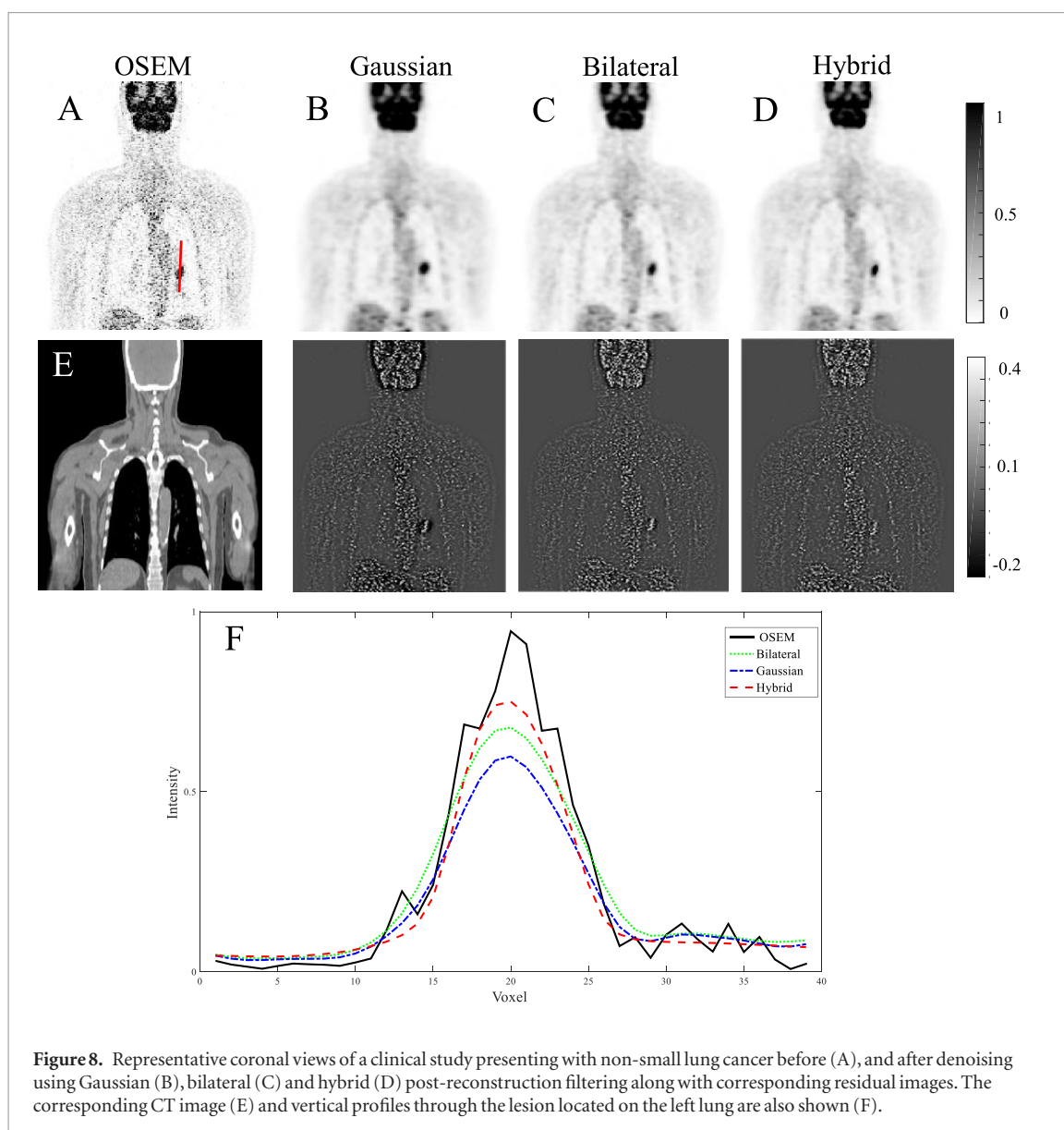
Figure 8. Representative coronal views of a clinical study presenting with non-small lung cancer before (A), and after denoising using Gaussian (B), bilateral (C) and hybrid (D) post-reconstruction filtering along with corresponding residual images. The corresponding CT image (E) and vertical profiles through the lesion located on the left lung are also shown (F).

Table 5. Contrast-to-noise ratio (CNR), signal-to-noise ratio (SNR), average lesion activity concentration (standard deviation) and quantification bias measured on ROIs defined on lesions for the clinical studies.

	OSEM	Gaussian	Bilateral	Hybrid
CNR	11.3	12.6	17.1	21.8
SNR	14.9	36.7	41.1	51.6
Average lesion activity concentration (kBq ml^{-1}) (SD)	13.3 (3.5)	11.4 (1.5)	12.1 (1.4)	12.9 (1.3)
Change (%)	—	−11.9	−6.6	−2.4

4. Discussion

In the proposed hybrid approach, the NLM filter was exploited to recover the strong features while smoothing out the low-contrast textures. As such, the filtering parameters should be optimized to preserve edges and high-contrast textures. Besides, a single set of NLM parameters may not be optimal to preserve both low- and high-contrast features concurrently. Conversely, the curvelet filter was optimized to suppress noise on the residual images which contain mostly low-contrast textures. Therefore, understanding the frequency range that each of the filter components is accountable for enables concurrent optimization of parameters, thus making noise discrimination feasible. For each component (low- or high-contrast), the range of frequencies that the filter should cope with is independent of the input image. As such, the frequency range of the input image does not necessarily need to be known. Regardless of the frequency content of the input image, the hybrid approach would smooth out each of the low- and high-frequency bands (if any) properly as there is a dedicated filtering

Figure 9. CNR values calculated for the lesion ROIs at different iteration numbers before (unfiltered OSEM) and after post-reconstruction filtering.

component for each frequency band. Denoising approaches rely on multiple parameters to determine the degree of smoothness or preservation of the target signal where one set of parameters may not satisfy the desirable outcome because of the variation in signal to noise ratio within or across images (Chan *et al* 2009). Parameter optimization is considerably less challenging in this hybrid approach since different denoising algorithms and set of parameters are applied sequentially for high- and low-contrast patterns. This adds to the robustness of the hybrid approach as it is applied on different sets of PET images.

Denoising approaches implemented in the transform domain sometimes suffer from ring artefacts near steep edges (Mulla *et al* 2013). This phenomenon is due to Gibbs effect since the coefficients for the high frequency content of the image are eliminated during noise cancellation and image formation processes. In the hybrid approach, the high frequency content of the image is processed by the NLM filter and the residual image (after subtraction of the NLM filtered image from the noisy image) which dominantly contains low-contrast structures is passed through the curvelet transform. Since there are no steep edges in the residual image, the curvelet transform did not generate any significant ring artefacts.

Most edge-preserving denoising approaches have a nonlinear behaviour and, as such, their performance depends on the lesion-to-background contrast. To evaluate the contrast dependency, three lesions with varying contrasts were simulated in a thorax phantom where the low contrast lesion is representative of low metabolic pulmonary lesions. The results reported in table 2 demonstrated that the hybrid method outperformed consistently conventional Gaussian and bilateral filters in terms of SNR and signal loss regardless of the contrast. When a sufficient contrast is present, the NLM filter can effectively detect and preserve prominent signal in the spatial domain while subtle noise is removed from the other regions by means of the curvelet filter. A minimum bias occurred when using the hybrid approach with dramatic improvement of the SNR and CNR. Likewise, the residual images of the clinical study shown in figure 8 and supplementary figure 4 demonstrated signal loss when using Gaussian and bilateral filters while the hybrid approach suppressed the noise at the cost of minimal change in signal with respect to the OSEM reconstructions.

The combination of spatial and transform domain filters achieved synergy as hybrid filtering exhibited higher SNR and lower bias or signal loss when compared to each of NLM and curvelet filters individually (table 1 and figure 5). The curvelet filter led to relatively low bias compared to NLM filter at the cost of poor noise removal as the SNR after curvelet filtering did not improve drastically.

Considering the experimental phantom, the Gaussian filter resulted in considerable signal loss when the size of the lesion decreases (table 3), whereas the edge preserving bilateral filter yielded lower signal loss owing to penalization of the smoothing factors over strong edges. In all cases, regardless of the denoising algorithm, a correlation was observed between the size of the target region and the resulting bias. The results suggest that the hybrid approach generates the highest SNR increase while minimizing signal loss. Noticeable amount of target signal is observed in the residual images using Gaussian and bilateral filtering regardless of the noise intensity. Since the hybrid approach yielded much less signal loss, in the case of high level of noise (short acquisition time), the target signal in the residual images was buried under the noise (figure 6). Similar phenomena were observed in the clinical studies where the standard deviation of lesions tracer uptake (table 5) have similar order of magni-

tude while producing dramatically different changes (%). Figure 8 and supplementary figure 4 further confirm this issue as the residual images exhibit similar noise reduction but different signal loss with respect to OSEM image. In some cases, the bilateral and hybrid filtered images do not exhibit substantial difference through visual inspection (e.g. figure 8) where even the residual images do not depict considerable differences. However, the line profile along with the lower signal loss and improved CNR scores demonstrated the overall quantitative gain achieved by the hybrid approach. The lesions portrayed in the clinical study present with different size and contrast with respect to the background. As such, the results presented in table 5 may not be directly comparable to spheres/lesions with specific sizes in the simulation or experimental studies.

In the case of high noise level, edge-preserving methods may treat the factitious features as genuine signals and, as such, they cannot properly smooth out these features. This case is seen in figure 6 when using the hybrid approach with 10 s acquisition time: certain noise-driven patterns in the largest sphere were not eliminated after filtration. In this case, the Gaussian filter resulted in visually superior image quality. Although the smallest sphere in the 10 s image on the slice shown in figure 6 appears to be better depicted than on the corresponding 30 s image, this observation is not reflected in the whole 3D volume. Similar to the largest sphere, the noise in the smallest sphere may be considered as a true signal further boosted by the edge preserving filter.

The proposed hybrid approach provides an insight regarding the successive application of two filters combining two domains, each one responsible for recovering features of different contrast levels. The noise cancellation in each domain is achieved more effectively as the target frequency range in the input signal is known, thus facilitating the parameters optimization process. Filtering parameter optimization and fine tuning could be achieved more effectively when the frequency response of the filter is limited independent of the frequency content of the input image. These features make the hybrid approach a versatile tool for denoising of PET images with different tracers presenting with various spatial and temporal distributions, For instance, in dynamic or low-dose PET imaging (Karakatsanis *et al* 2016, Yan *et al* 2016, Rahmim *et al* 2018) where the low SNR induces severe bias and large variance in estimates of physiological parameters, image denoising capable of preserving the spatial resolution and quantitative accuracy is highly desirable. In this regard, the hybrid approach appears to be an effective denoising technique owing to its relatively high quantitative accuracy and improved SNR. Furthermore, dynamic frame-by-frame PET imaging tends to use shorter time bins to track rapid changes in the radiotracer concentration and thus be able to sample adequately the early peak of the input function (Zanotti-Fregonara 2009). As a result, dynamic PET images corresponding to early frames suffer from poor photon statistics and tend to be substantially nosier. Since there might be differences in noise levels from one frame to another in dynamic PET imaging (Boellaard *et al* 2001), a denoising approach supporting the broad range of noise levels is mandatory. In order to facilitate the clinical adoption of the proposed method, its clinical assessment should be performed by expert physicians. Moreover its robustness should be further evaluated using a different larger clinical database with variable characteristics (different injected doses, acquisition times, noise levels, different tracers, …etc) to spot any drawbacks and above all any potential artefacts that might adversely impact clinical PET. Similar to other edge preserving techniques, non-optimal parameter selection for the hybrid filters, artefacts might appear in the case of high noise levels. When the noise amplitude competes with the underlying signal, edge preserving filters might consider it as genuine signal and as such, the noise would remain intact in the final image.

The selection and combination of filters play a crucial role in this approach where complementary filtering algorithms (low/high contrast or spatial/frequency domain) can bring synergy into this approach. The combination of NLM and curvelet filters achieved promising results as post-processing tools in whole-body PET studies. However, in certain applications, such as denoising of natural images or structural images (CT or MRI) where the noise characteristics are different from typical PET images, other variants of hybrid filtering would lead to comparable outcome (Pierazzo and Facciolo 2017). Variants of hybrid filtering can be implemented through a different combination of filters in the spatial and/or frequency domains. Another potential avenue is the iterative implementation of the proposed approach where, at each iteration, a certain frequency range of the input image is processed to enhance the overall performance of the filter. Since the proposed hybrid approach is not computationally demanding (15 s for a whole-body PET image), iterative implementation of the proposed method (e.g. on a multi-core processor) is feasible.

5. Conclusion

A novel denoising approach for PET images was presented, combining the advantages of spatial and frequency domain filtering to effectively suppress noise while minimizing signal loss and quantification bias. The proposed technique is based on the combination of a NLM filter (spatial domain) and the curvelet transform as a multi-resolution technique (frequency domain) implemented in a sequential filtering scheme. Spatial domain filtering predominantly recovers the high contrast features whereas frequency domain filtering preserves the remaing low contrast textures during the denoising process. The simulated, experimental and clinical PET studies demonstrated that the proposed approaches outperformed conventional Gaussian and edge preserving bilateral

denoising techniques. The hybrid denoising approach is promising (when filtering parameters are properly optimized) and could replace conventional Gaussian filtering since it provides superior noise cancellation and signal preservation.

Acknowledgments

ORCID iDs

Habib Zaidi ⓘ https://orcid.org/0000-0001-7559-5297

References

Boashash B 2015 *Time-Frequency Signal Analysis and Processing: a Comprehensive Reference* (New York: Academic)

Boellaard R, van Lingen A and Lammertsma A A 2001 Experimental and clinical evaluation of iterative reconstruction (OSEM) in dynamic PET: quantitative characteristics and effects on kinetic modeling *J. Nucl. Med.* **42** 808–17

Brox T, Kleinschmidt O and Cremers D 2008 Efficient nonlocal means for denoising of textural patterns *IEEE Trans. Image Process.* **17** 1083–92

Buades A, Coll B and Morel J-M 2005 A non-local algorithm for image denoising *2005 IEEE Computer Society Conf. on Computer Vision and Pattern Recognition (CVPR'05) Series 2* pp 60–5

Chan C, Fulton R, Barnett R, Feng D D and Meikle S 2014 Postreconstruction nonlocal means filtering of whole-body PET with an anatomical prior *IEEE Trans. Med. Imaging* **33** 636–50

Chan C, Fulton R, Feng D D and Meikle S 2009 Regularized image reconstruction with an anatomically adaptive prior for positron emission tomography *Phys. Med. Biol.* **54** 7379–400

Dettori L and Semler L 2007 A comparison of wavelet, ridgelet, and curvelet-based texture classification algorithms in computed tomography *Comput. Biol. Med.* **37** 486–98

Donoho D L and Johnstone J M 1994 Ideal spatial adaptation by wavelet shrinkage *Biometrika* **81** 425–55

Easley G, Labate D and Lim W-Q 2008 Sparse directional image representations using the discrete shearlet transform *Appl. Comput. Harmon. Anal.* **25** 25–46

Elad M 2002 On the origin of the bilateral filter and ways to improve it *IEEE Trans. Image Process.* **11** 1141–51

Guo H, Renaut R, Chen K and Reiman E 2003 Clustering huge data sets for parametric PET imaging *Biosystems* **71** 81–92

Hofheinz F, Langner J, Beuthien-Baumann B, Oehme L, Steinbach J, Kotzerke J and van den Hoff J 2011 Suitability of bilateral filtering for edge-preserving noise reduction in PET *EJNMMI Res.* **1** 23

Hyder S A and Sukanesh R 2011 *Software Tools and Algorithms for Biological Systems* (Berlin: Springer) pp 471–80

Karakatsanis N A, Casey M E, Lodge M A, Rahmim A and Zaidi H 2016 Whole-body direct 4D parametric PET imaging employing nested generalized Patlak expectation–maximization reconstruction *Phys. Med. Biol.* **61** 5456–85

Kim J H, Ahn I J, Nam W H and Ra J B 2015 An effective post-filtering framework for 3D PET image denoising based on noise and sensitivity characteristics *IEEE Trans. Nucl. Sci.* **62** 137–47

Knaus C and Zwicker M 2013 Dual-domain image denoising *IEEE Int. Conf. on Image Processing (ICIP)* pp 440–4

Knaus C and Zwicker M 2014 Progressive image denoising *IEEE Trans. Image Process.* **23** 3114–25

Le Pogam A, Hanzouli H, Hatt M, Le Rest C C and Visvikis D 2013 Denoising of PET images by combining wavelets and curvelets for improved preservation of resolution and quantitation *Med. Image Anal.* **17** 877–91

Lehovich A, Bruyant P P, Gifford H S, Schneider P B, Squires S, Licho R, Gindi G and King M A 2009 Impact on reader performance for lesion-detection/localization tasks of anatomical priors in SPECT reconstruction *IEEE Trans. Med. Imaging* **28** 1459–67

Mohammed J R 2008 An improved median filter based on efficient noise detection for high quality image restoration *IEEE Second Asia Int. Conf. (AICMS)* pp 327–31

Mulla A, Patil A, Pethkar S and Deshmukh N 2013 A comparative study of different image denoising methods *Int. J. Innov. Res. Sci. Eng. Technol.* **2** 737–43

Nuyts J, Baete K, Beque D and Dupont P 2005 Comparison between MAP and postprocessed ML for image reconstruction in emission tomography when anatomical knowledge is available *IEEE Trans. Med. Imaging* **24** 667–75

Nuyts J and Fessler J A 2003 A penalized-likelihood image reconstruction method for emission tomography, compared to postsmoothed maximum-likelihood with matched spatial resolution *IEEE Trans. Med. Imaging* **22** 1042–52

Paris S, Kornprobst P, Tumblin J and Durand F 2009 Bilateral filtering: theory and applications *Found. Trends® Comput. Graph. Vis.* **4** 1–73

Perona P and Malik J 1990 Scale-space and edge detection using anisotropic diffusion *IEEE Trans. Pattern Anal. Mach. Intell.* **12** 629–39

Pierazzo N and Facciolo G 2017 Data adaptive dual domain denoising: a method to boost state of the art denoising algorithms *Image Process. Line* **7** 93–114

Pierazzo N, Lebrun M, Rais M, Morel J-M and Facciolo G 2014 Non-local dual image denoising *IEEE Int. Conf. Image Processing (ICIP)* pp 813–7

Qi J and Leahy R M 2006 Iterative reconstruction techniques in emission computed tomography *Phys. Med. Biol.* **51** R541–78

Rahmim A, Lodge M, Karakatsanis N, Panin V, Zhou Y, McMillan A, Cho S, Zaidi H, Casey M and Wahl R 2018 Dynamic whole-body PET imaging: principles, potentials and applications *Eur. J. Nucl. Med. Mol. Imaging* (accepted) (https://doi.org/10.1007%2Fs00259-018-4153-6)

Reader A J and Zaidi H 2007 Advances in PET image reconstruction *PET Clinics* **2** 173–90

Sawatzky A, Brune C, Wubbeling F, Kosters T, Schafers K and Burger M 2008 Accurate EM-TV algorithm in PET with low SNR *IEEE Nuclear Science Symp. Conf. Record* pp 5133–7

Sendur L and Selesnick I W 2002 Bivariate shrinkage with local variance estimation *IEEE Signal Process. Lett.* **9** 438–41

Shan H, Ma J and Yang H 2009 Comparisons of wavelets, contourlets and curvelets in seismic denoising *J. Appl. Geophys.* **69** 103–15

Shih Y-Y, Chen J-C and Liu R-S 2005 Development of wavelet de-noising technique for PET images *Comput. Med. Imaging Graph.* **29** 297–304

Shukla M and Changlani S 2013 A comparative study of wavelet and curvelet transform for image denoising *IOSR J. Electron. Commun. Eng.* **7** 63–8

Snyder D L, Miller M I, Thomas L J and Politte D G 1987 Noise and edge artifacts in maximum-likelihood reconstructions for emission tomography *IEEE Trans. Med. Imaging* **6** 228–38

Starck J-L, Candès E J and Donoho D L 2002 The curvelet transform for image denoising *IEEE Trans. Image Process.* **11** 670–84

Turkheimer F E, Banati R B, Visvikis D, Aston J A, Gunn R N and Cunningham V J 2000 Modeling dynamic PET-SPECT studies in the wavelet domain *J. Cereb. Blood Flow Metab.* **20** 879–93

Vunckx K, Atre A, Baete K, Reilhac A, Deroose C M, Van Laere K and Nuyts J 2012 Evaluation of three MRI-based anatomical priors for quantitative PET brain imaging *IEEE Trans. Med. Imaging* **31** 599–612

Yan J, Schaefferkoetter J, Conti M and Townsend D 2016 A method to assess image quality for low-dose PET: analysis of SNR, CNR, bias and image noise *Cancer Imaging* **16** 26

Zanotti-Fregonara P, Fadaili el M, Maroy R, Comtat C, Souloumiac A, Jan S, Ribeiro M J, Gaura V, Bar-Hen A and Trebossen R 2009 Comparison of eight methods for the estimation of the image-derived input function in dynamic [(18)F]-FDG PET human brain studies *J. Cereb. Blood Flow Metab.* **29** 1825–35